PNAS RESEARCH ARTICLE | EARTH, ATMOSPHERIC, AND PLANETARY SCIENCES

Sensitivity of mass-independent Sn isotope fractionation to UV radiation and magnetic fields

Jia-Xin She[a,b], Weiqiang Li[a,b,1], Shujuan Zhang[c,d], Cheng Gu[c,d], Xiru Chen[c,d], Hongcen Zheng[c,d,e], Cheng Xu[a,b], and Wei Liu[a,b]

Edited by Mark Thiemens, University of California San Diego, La Jolla, CA; received February 20, 2025; accepted May 7, 2025

Mass-independent isotope fractionation (MIF) enables powerful geochemical tracers for various geological and planetary problems, yet the mechanisms driving MIF for tin (Sn) remain ambiguous. Here, we demonstrate that distinct Sn isotope fractionation signatures were produced during photolysis of organic Sn species (i.e., methyltin) under laboratory UV irradiation and natural sunlight. UV irradiation of methyltin induced pronounced Sn-MIF in all odd Sn isotopes (Δ^{115}Sn up to 21.82‰, Δ^{117}Sn up to 23.16‰, Δ^{119}Sn up to 24.01‰), with their ratios ($\Delta^{117}Sn/\Delta^{115}Sn = 1.069$; $\Delta^{119}Sn/\Delta^{115}Sn = 1.099$; $\Delta^{119}Sn/\Delta^{117}Sn = 1.028$) strongly correlating with nuclear magnetic moments. This unambiguously identifies the magnetic isotope effect (MIE) as the driving mechanism, ruling out other causes such as the nuclear volume effect (NVE). Methyl radicals ($\bullet CH_3$) were detectable during the methyltin photolysis experiments, and the magnitude of MIF for Sn was suppressed by the presence of electron spin trapping agent (DMPO) for radicals, supporting that the pronounced Sn-MIF originated from radical-mediated singlet-triplet state transitions of Sn species. Furthermore, the magnitude of Sn-MIF depended nonmonotonically on external magnetic fields (peak suppression at 100 to 180 G), implying competition between hyperfine coupling and Zeeman interactions. Notably, Sn-MIF was absent during photolysis of methyltin by natural sunlight despite significant mass-dependent Sn isotope fractionation (e.g., >3‰ in $\delta^{122/116}$Sn), attributed to atmospheric ozone shielding of short-wavelength UV (<290 nm) required for radical generation. Our results register Sn-MIF as a sensitive tracer of UV-driven photochemistry in low-oxygen environments, underlining the potential of Sn isotopes in studies of early Earth's atmosphere and planetary environments.

magnetic isotope effect | tin isotopes | mass-independent fractionation | photochemistry | magnetic fields

Significance

This study provides compelling evidence that UV irradiation significantly induces mass-independent fractionation (MIF) in odd Sn isotopes ($^{115, 117, 119}$Sn) via the magnetic isotope effect (MIE), a process facilitated by radical pairs and modulated by magnetic fields. Importantly, the absence of Sn-MIF under natural sunlight indicates that the mass dependency of Sn isotope fractionation is particularly sensitive to UV wavelengths filtered by Earth's ozone layer. This unique signature of MIE of Sn can be distinguished from other sources of MIF, making Sn-MIF a potential tracer for photochemical reactions in Archean Earth and extraterrestrial materials.

The magnetic isotope effect (MIE) offers a unique window into reaction mechanisms in Earth and environmental sciences (1, 2). MIE arises when magnetic nuclei generate internal magnetic fields around unpaired electrons in reactive paramagnetic species, leading to reactivity differences compared to species with nonmagnetic nuclei (3). Unlike the classical mass-dependent isotope effect, the MIE exhibits several distinguishing features: The MIE operates only in reactions involving radical pair (RP) formation and recombination; the MIE can reach tens of per mil (‰) in magnitude, significantly higher than classical mass-dependent isotope effects; the MIE depends on the hyperfine energy, the spins and magnetic moments of the nuclei, and parameters characterizing the radical pair molecular dynamics (4); the MIE exhibits a strong dependency on magnetic fields, unlike the classical mass-dependent isotope effect, which remains insensitive to magnetic fields (4, 5).

Tin (Sn), as the only element in the periodic table that has three stable magnetic isotopes [^{115}Sn, ^{117}Sn, ^{119}Sn (I = 1/2)], holds remarkable potential for tracing Sn cycling through mass-independent Sn isotope fractionation (Sn-MIF). Sn-MIF has been identified in meteorites (6), but the mechanisms underlying the observed fractionation patterns remain unclear. An early liquid extraction experiment of $SnCl_2$ with crown ether reported significant Sn-MIF and attributed it to the nuclear volume effect (NVE) (7), while MIE was suggested in other photochemical experimental studies (8, 9). Recently, Fukami et al. (10) argued, based on the relationships between MIF of ^{117}Sn and ^{119}Sn (i.e., $\Delta^{119}Sn/\Delta^{117}Sn$ of 1.082), that liquid extraction experiments of $SnCl_2$ with crown ether involved MIE, with additional subtle MIF signatures in even isotopes (^{118}Sn, ^{122}Sn, ^{124}Sn) caused by NVE. However, the pioneering photochemical experiments of Malinovskiy et al. (8) showed a wide range (0.881 to 1.031) in $\Delta^{119}Sn/\Delta^{117}Sn$, which cannot be satisfactorily explained using the approach of Fukami et al. (10) for MIE.

Despite the discovery of Sn-MIF in the above experimental studies, the detailed mechanisms causing the Sn-MIF remain elusive, with several key aspects unresolved:

Author affiliations: [a]State Key Laboratory of Critical Earth Material Cycling and Mineral Deposits, School of Earth Sciences and Engineering, Nanjing University, Nanjing, Jiangsu 210023, China; [b]Frontiers Science Center for Critical Earth Material Cycling, Nanjing University, Nanjing, Jiangsu 210023, China; [c]School of Environment, Nanjing University, Nanjing, Jiangsu 210023, China; [d]State Key Laboratory of Water Pollution Control and Green Resource Recycling, School of the Environment, Nanjing University, Nanjing 210023, China; and [e]Nanjing Institute of Environmental Sciences, Ministry of Ecology and Environment of the People's Republic of China, Nanjing, Jiangsu 210042, China

Author contributions: J.-X.S. and W.L. designed research; J.-X.S., W.L., C.X., and W.L. performed research; J.-X.S., W.L., S.Z., C.G., X.C., and H.Z. contributed new reagents/analytic tools; J.-X.S., W.L., S.Z., and C.G. analyzed data; and J.-X.S. and W.L. wrote the paper.

The authors declare no competing interest.

This article is a PNAS Direct Submission.

[1]To whom correspondence may be addressed. Email: liweiqiang@nju.edu.cn.

This article contains supporting information online at https://www.pnas.org/lookup/suppl/doi:10.1073/pnas.2504065122/-/DCSupplemental.

Published June 12, 2025.

1) In theory, if MIE takes place, MIF should occur to all of the magnetic isotopes (^{115}Sn, ^{117}Sn, ^{119}Sn), yet earlier investigations only reported MIF of ^{117}Sn and ^{119}Sn (7, 8, 10), thus the MIF of ^{115}Sn remains to be confirmed; 2) MIE is often ascribed to radical-mediated reaction mechanisms, yet the presence and effects of radicals have not been conclusively demonstrated in previous experiments; 3) MIE should show dependence to magnetic field strength (5, 11), however, there has been no experimental confirmation for Sn isotopes; 4) Photochemical transformations of organotin species is ubiquitous for Sn cycling in the natural environment (12, 13), yet no experimental investigation has been made on Sn-MIF under natural sunlight conditions.

To bridge these gaps, we designed a systematic experimental campaign targeting the interplay between photochemistry, MIE, and radical dynamics in Sn-MIF generation. Our study has made four notable advancements: 1) By integrating high-precision ^{115}Sn measurements with existing ^{117}Sn and ^{119}Sn data, we rigorously test whether MIE universally affects all magnetic isotopes; 2) Using spin-trapping agents (e.g., DMPO) and in situ radical detection, we directly assess radical involvement in singlet-triplet transitions underlying MIE; 3) Through controlled magnetic field experiments, we establish the experimental correlation between Sn-MIF magnitude and external field strength, testing theoretical predictions; 4) By replicating natural sunlight spectra, we disentangle wavelength-specific MIE, bridging lab-based mechanisms to geological Sn cycling. Collectively, this work clarifies the origin of Sn-MIF and establishes its utility as a probe for reconstructing photochemical regimes in planetary environments, from early Earth systems to extraterrestrial materials.

Results

In this study, three distinct photolysis experiments were performed on CH_3SnCl_3, or methyltin (*SI Appendix*, Fig. S1). Standard photolysis experiments were conducted under the Earth's natural magnetic field (~0.5 G), utilizing a Hg lamp or sunlight as the irradiation source. In a different set of experiments, DMPO, a type of electron spin trap agent, was added to the aqueous solution. In a third set of experiments, the UV photolysis of CH_3SnCl_3 took place under different magnetic fields, varying from 0.002 to 3255 G. In all experiments, the aqueous solutions were sampled in time series (*SI Appendix*, Figs. S2 and S3), followed by separation of the inorganic and organic Sn species by ion exchange and subsequent elemental and Sn isotopic analyses. Sn isotope compositions are reported in δ values relative to the primary Sn isotopic reference solution NIST 3161a, as $\delta^{y/116}Sn3161a = [(^{y}Sn/^{116}Sn)_{sample}/(^{y}Sn/^{116}Sn)_{3161a} - 1] \times 1{,}000$. Mass-independent fractionation (MIF) of Sn is characterized using the "capital delta" notation, as $\Delta^{x/116}Sn = \delta^{x/116}Sn - [\ln(x/116)/\ln(120/116)] \times \delta^{120/116}Sn$, which is corrected for mass-dependent Sn isotope fractionation by $\delta^{120/116}Sn$ (14). Details regarding the experiments and analytical methods are provided in the *Materials and Methods* and *SI Appendix*.

Very large mass-independent Sn isotope fractionation occurred during UV-induced photolysis under Earth's magnetic field. Notably, MIF was exclusively observed for odd Sn isotopes (^{115}Sn, ^{117}Sn, ^{119}Sn), and no Sn-MIF was found for nonmagnetic isotopes (116, 118, 120, 122), as summarized in Fig. 1 and Dataset S1. The $\Delta^{115/116}Sn$ values varied widely from −13.08 to 8.74‰, covering an overall range of 21.82‰ ($\Delta^{117/116}Sn$ from −13.90 to 9.26‰, $\Delta^{119/116}Sn$ from −14.39 to 9.61‰) (Fig. 1). In contrast, the $\Delta^{118/116}Sn$ and $\Delta^{122/116}Sn$ values of the same samples varied from −0.03 to 0.04‰ and −0.10 to 0.11‰, equal to 0‰ within analytical uncertainties (Dataset S1). Despite that, the mass-dependent Sn isotope fractionations were also significant, such that the $\delta^{122/116}Sn_{3161a}$ values of the samples ranged from −3.58 to 0.59‰ ($\delta^{120/116}Sn_{3161a}$ ranging from −2.43 to 0.39‰, proportionally to mass difference). Notably, samples showing negative $\Delta^{115/116}Sn$ values generally had negative $\delta^{122/116}Sn_{3161a}$ values, and vice versa, thus the majority of the photochemical experimental data points appeared in the first and third quadrants of the plot of $\delta^{122/116}Sn$ versus $\Delta^{115/116}Sn$ (Fig. 1).

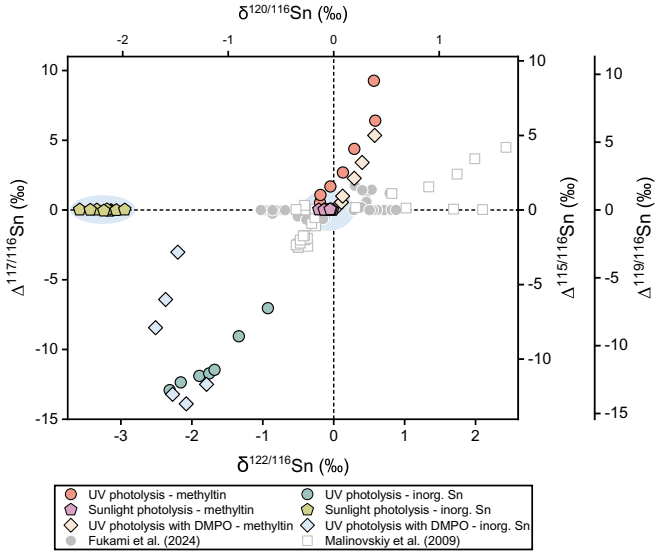

Fig. 1. The plot of $\Delta^{117/116}Sn$, $\Delta^{115/116}Sn$, and $\Delta^{119/116}Sn$ versus $\delta^{122/116}Sn$ and $\delta^{120/116}Sn$ for samples from photolysis experiments under the Earth's natural magnetic field. The photolysis experiments include three different conditions: UV-only photolysis (PR 2), UV photolysis in the presence of DMPO (PR 68), and photolysis under sunlight (PR 42). *Right* axes are scaled to reflect the experimentally determined slopes of $\Delta^{117/116}Sn$, $\Delta^{119/116}Sn$, and $\Delta^{115/116}Sn$ (this study) and apply exclusively to the data from this work. Dotted lines mark $\Delta^{115/116}Sn = 0$ and $\delta^{122/116}Sn_{3161a} = 0$ for visual reference. The blue-shaded region highlights data from sunlight photolysis experiments. Data from prior studies (8, 10) are included for comparison. Note: $\delta^{122/116}Sn$ values from Malinovskiy (8) are reported relative to their in-house isotopic standard and are not directly normalized to the reference standard used in this work.

During UV photolysis of organic Sn, the reactants (CH_3SnCl_3) were enriched in heavy Sn isotopes, with $\delta^{122/116}Sn$ and $\Delta^{115/116}Sn$ increasing with time (Fig. 2*A*), correspondingly, the reaction products (inorganic Sn) were enriched in light Sn isotopes (i.e., negative $\delta^{122/116}Sn$ and $\Delta^{115/116}Sn$) (Fig. 2*A*). Upon the addition of DMPO to the aqueous solution during UV photolysis of organic Sn, the Sn-MIF was greatly suppressed (i.e., the difference in $\Delta^{115/116}Sn$ between organic and inorganic Sn was <3.10‰ in the first sample pair), but with increasing time, the difference in $\Delta^{115/116}Sn$ between organic and inorganic Sn increased to up to 16.56‰. However, the mass-dependent fractionation (MDF) of Sn isotopes was not affected, with an evolution pattern similar to that of UV photolysis experiment without DMPO (Fig. 2*B*). The more striking finding from our experiments is the absence of detectable MIF during photochemical experiments exposed to natural sunlight (Fig. 2*C*), despite the significant MDF (difference in $\delta^{122/116}Sn_{3161a}$ between the product and reactant ranged from −2.81 to −3.45‰) observed under these conditions (Figs. 1 and 2*C*). The $\Delta^{115/116}Sn$ values of photochemical samples from sunlight irradiation ranged narrowly from −0.12 to 0.10‰ ($\Delta^{117/116}Sn$ of −0.06 to 0.05‰, $\Delta^{119/116}Sn$ of −0.08 to 0.10‰), equal to 0‰ within analytical uncertainties. Sunlight-derived experiments can be distinguished from UV experiments based on their distinct coupled mass-dependent and mass-independent relationships (Fig. 1).

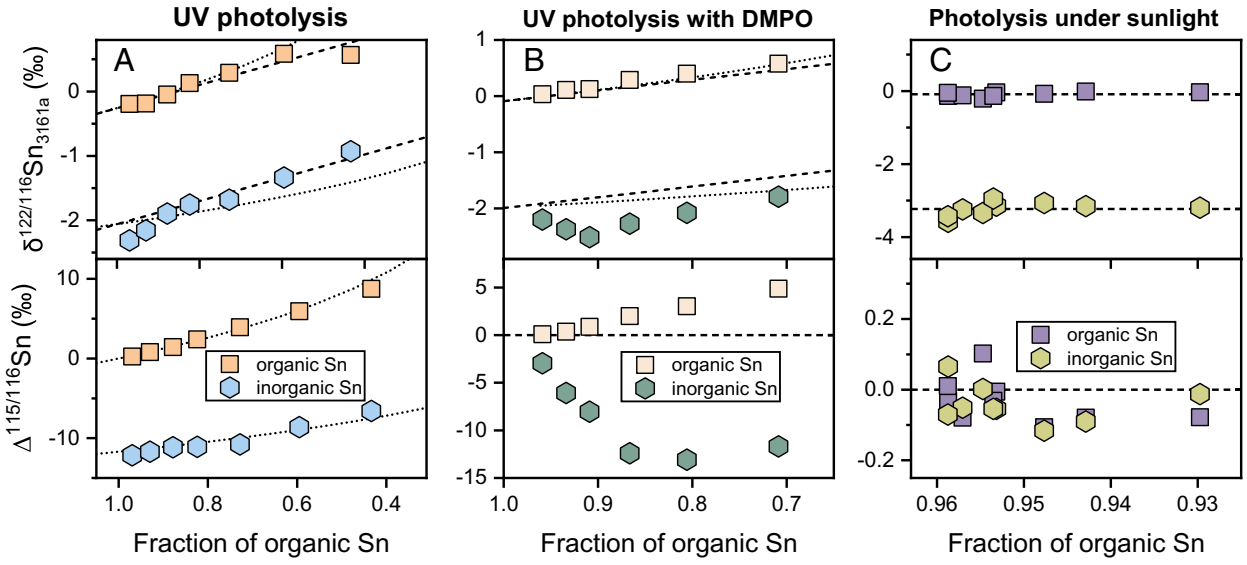

Fig. 2. Plots of $\delta^{122/116}Sn_{3161a}$ and $\Delta^{115/116}Sn$ values as a function of organic Sn proportion for various photolysis experiments under the Earth's natural magnetic field. (*A*) UV-induced photolysis experiment (PR 2). Dotted and dashed lines represent predictions from the Rayleigh and equilibrium fractionation models, respectively. (*B*) UV-induced photolysis experiment with 10 mg of DMPO (5,5-dimethyl-1-pyrroline N-oxide) added (PR 68). Dotted and dashed lines for $\delta^{122/116}Sn_{3161a}$ indicate predictions from the Rayleigh and equilibrium fractionation models, respectively. A dashed line at $\Delta^{115/116}Sn = 0$ serves as a reference for no isotopic fractionation. (*C*) Sunlight-induced photolysis experiment (PR 42). Dashed lines for $\delta^{122/116}Sn_{3161a}$ represent the average compositions of organic and inorganic Sn. A dashed line at $\Delta^{115/116}Sn=0$ indicates no isotopic fractionation between reactants and products.

The general Sn isotope behaviors during photolysis of CH_3SnCl_3 under variable magnetic field strengths were similar to that in standard photolysis experiments under Earth's natural magnetic field, in terms of 1) both MIF and MDF of Sn isotopes occurred upon UV irradiation and light Sn isotopes were enriched in the reaction products (inorganic Sn), 2) MIF only occurred to odd Sn isotopes (^{115}Sn, ^{117}Sn, ^{119}Sn). However, the reaction kinetics of methyltin photolysis differed under different magnetic field strengths (Fig. 3*C* and *SI Appendix*, Fig. S3), and the magnitude of MIF varied as well. The magnitude of MIF can be quantified by the difference in $\Delta^{115/116}Sn$ values between the residual methyltin and the reaction products of inorganic Sn (i.e., $\Delta^{115/116}Sn_{org.-inorg.}$). The maximum $\Delta^{115/116}Sn_{org.-inorg.}$ value reached ~13‰ under Earth's natural magnetic field (0.5 G) or inside a paleomagnetic laboratory (0.002 G). The maximum $\Delta^{115/116}Sn_{org.-inorg.}$ during methyltin photolysis was suppressed to <4‰ under the magnetic field strength of 50 to 200 G, but was elevated again to >4‰ under magnetic field strength of 444 G and above (Fig. 3*A*). Experiments showed the least MIF of Sn under magnetic field strength of 100 to 180 G (Fig. 3*A*). It should be noted that the magnitude of MDF of Sn isotopes was similar in all photolysis experiments regardless of magnetic field strength (Fig. 3*B* and Dataset S2).

Discussion

Detection of MIF on ^{115}Sn under UV Irradiation. One of the key findings of this study is the very large MIF observed exclusively in all odd Sn isotopes (^{115}Sn, ^{117}Sn, ^{119}Sn) during UV-driven photochemical experiments. Several mechanisms have been proposed to account for the occurrence of MIF, including differences in molecular symmetry (15, 16), NVE (17), magnetic effect (5), and the difference between kinetic and equilibrium MDF (10). Symmetry effect, the difference between kinetic and equilibrium MDF, and NVE theoretically could lead to MIF on odd Sn isotopes, however, they would also produce significant MIF on even isotopes (e.g., ^{118}Sn, ^{122}Sn, and ^{124}Sn) (10, 18), which are absent in our experiments. The NVE of Sn isotopes had been reported from liquid extraction experiments (7, 10), during which chelation by macrocyclic ligands could be sensitive to nuclear radius differences. But chelation is absent during photolysis processes, as shown in this study and the study of Malinovskiy et al. (8). Additionally, the magnitude of Sn-MIF observed in our photochemical experiments (>23‰ in $\Delta^{117}Sn$) far exceeds the magnitude of Sn-MIF predicted for NVE (i.e., <0.5‰ in $\Delta^{117}Sn$) (10, 19, 20). Therefore, MIE is left as the most probable cause of the observed Sn isotope data in our study.

One remarkable feature of the Sn isotope data in this study is the highly uniform proportionality of MIF signatures among the three odd Sn isotopes. All samples plot along linear trends on plots of $\Delta^{117/116}Sn$ vs. $\Delta^{115/116}Sn$, $\Delta^{119/116}Sn$ vs. $\Delta^{115/116}Sn$, and $\Delta^{119/116}Sn$ vs. $\Delta^{117/116}Sn$, defining ratios of 1.069, 1.099, and 1.028 for $\Delta^{117}Sn/\Delta^{115}Sn$, $\Delta^{119}Sn/\Delta^{115}Sn$, and $\Delta^{119}Sn/\Delta^{117}Sn$, respectively (Fig. 4 *A*–*C*). For comparison, the ratios of nuclear magnetic moments (μ_n) between the odd Sn isotope pairs are 1.089 for $^{117}Sn/^{115}Sn$, 1.140 for $^{119}Sn/^{115}Sn$, and 1.046 for $^{119}Sn/^{117}Sn$. The close correlation between the ratios of MIF signatures and the ratios of nuclear magnetic moments between the three odd Sn isotopes strongly suggests the dominant control of MIE. The MIE leverages the nuclear magnetic moments and nonzero magnetic spin of reactants to modulate reaction rates, resulting in enhanced fractionation of odd-mass Sn isotopes ($^{115,117,119}Sn$) (10). The ratios of $\Delta^{117}Sn/\Delta^{115}Sn$, $\Delta^{119}Sn/\Delta^{115}Sn$, and $\Delta^{119}Sn/\Delta^{117}Sn$ caused by MIE could be theoretically predicted, and can vary due to the relative lengths of the spin conversion time and radical lifetime in specific reactions (3, 10). Similarly, the symmetry effect, difference between kinetic and equilibrium MDF, and NVE could also result in characteristic ratios $\Delta^{117}Sn/\Delta^{115}Sn$, $\Delta^{119}Sn/\Delta^{115}Sn$, and $\Delta^{119}Sn/\Delta^{117}Sn$. When comparing the experimentally determined ratios of $\Delta^{117}Sn/\Delta^{115}Sn$, $\Delta^{119}Sn/\Delta^{115}Sn$, and $\Delta^{119}Sn/\Delta^{117}Sn$ with those predicted by MIE, symmetry effects, difference between kinetic and equilibrium MDF, and NVE (Fig. 4), it is clear that the experimental data plot within the MIE range, and the distinction between MIE and non-MIE mechanisms (e.g., NVE) are particularly pronounced for $\Delta^{117}Sn/\Delta^{115}Sn$ and $\Delta^{119}Sn/\Delta^{115}Sn$, compared to the $\Delta^{119}Sn/\Delta^{117}Sn$ as has been discussed recently for the liquid extraction experiments (10). Therefore, analysis of ^{115}Sn

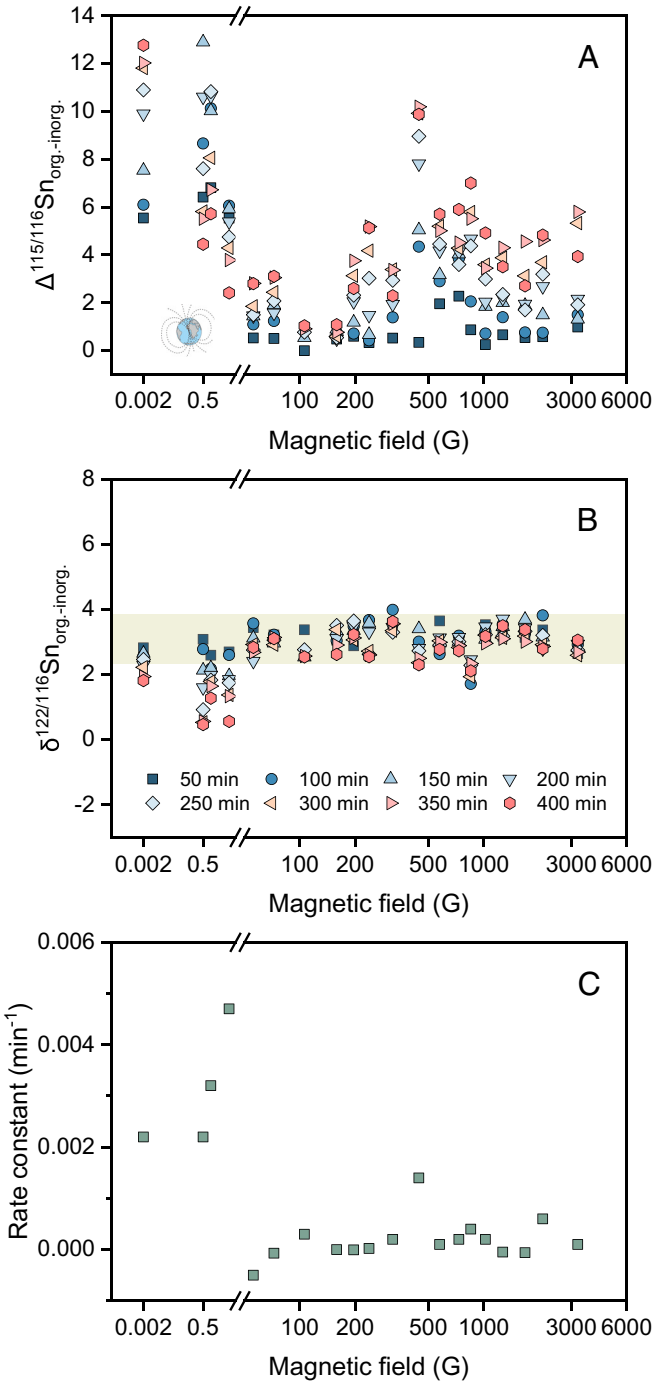

Fig. 3. (*A*) Magnetic field-induced $\Delta^{115/116}$Sn values between organic and inorganic Sn as a function of external magnetic field strength. (*B*) Variations in $\delta^{122/116}$Sn difference between organic and inorganic Sn under different external magnetic fields. The shaded area represents the average $\delta^{122/116}Sn_{org.-inorg.}$ value obtained at 50 min under various magnetic field conditions. Data points correspond to Sn isotope values from samples collected at different time intervals during the experiment. (*C*) Photolysis reaction rate constants are plotted as a function of magnetic field strength.

signatures can significantly enhance the sensitivity to discern MIE from other mechanisms for Sn isotopes.

The Effect of Radicals on MIF under UV Irradiation. According to the established theory of MIE, MIF during photochemical reactions arises from spin-selective recombination of radical pairs (4, 5, 23). In our photolysis experiments, the primary intermediate is a triplet radical pair (SnX_3• •CH_3, X = Cl or OH) generated by UV-induced C-Sn bond cleavage (*SI Appendix*, Fig. S4). The fate of this pair depends on spin dynamics, including the formation of inorganic Sn (the product) and/or its recombination to regenerate the original methyltin molecule (CH_3Sn). Due to the general rule of spin-conservation and the constraint of radical recombination energy requirement, the recombination of the methyltin molecule is only possible for the product in a ground singlet state (4). To recombine and produce a zero-spin molecule CH_3Sn, triplet-singlet (T-S) spin conversion of the radical pair within its lifetime is required. Crucially, magnetic Sn isotopes ($^{115, 117, 119}$Sn) exhibit accelerated T-S conversion due to hyperfine coupling (HFC) between unpaired electrons and magnetic nucleus. In contrast, nonmagnetic Sn isotopes ($^{116, 118, 120, 122, 124}$Sn) lack significant HFC (except for subtle contributions from protons), leading to delayed T-S conversion and preferential dissociation into reaction products (inorganic Sn) (*SI Appendix*, Fig. S4). As such, the MIE theory satisfactorily explains the depletion of all odd isotopes of Sn in the photolysis products (inorganic Sn) with excellent proportionality to the magnetic moment of the nucleus.

Despite the effectiveness of MIE in explaining the experimental data, direct evidence for the existence of radicals has been lacking in previous experimental studies on Sn-MIF (7, 8, 10). Malinovskiy et al. (8) indirectly inferred the role of radicals in Sn-MIF signature generation, they reported the lack of Sn-MIF in photolysis experiments under high pH (~7.8) solutions, and explained it with inhibition of free radicals by hydroxyl anions (OH^-). In our study, we performed in situ electron spin resonance spectroscopy (ESR) during the methyltin photolysis experiment and obtained direct evidence of methyl radicals (Fig. 5), which reflected the cleavage of the C-Sn bond. More illuminating is our photolysis experiment with DMPO, in which the MIF was almost completely suppressed at the beginning of the experiment, followed by the gradual increase of MIF with time (Fig. 2*b*). This phenomenon aligns with DMPO's role: It traps transient radicals (forming stable adducts), reducing free radical concentration and collision probability, thereby inhibiting spin conversion and recombination (*SI Appendix*, Fig. S4). Subsequent UV exposure degraded DMPO-radical adducts (24), releasing radicals and restoring MIF (*SI Appendix*, Fig. S4). These results provide clear evidence for radical involvement in Sn-MIF.

Although Sn-MIF has been observed in both photochemical experiments (this study and ref. 8) and liquid extraction experiments (7, 10), the magnitude of MIF in our photochemical experiments is remarkably greater (>23‰ on Δ^{117}Sn versus < 2.5‰ in liquid extraction experiments) (Fig. 1), and the $\Delta^{119}Sn/\Delta^{117}Sn$ ratio of photochemical experiments in this study is smaller than that in the liquid extraction experiments of Fukami (10) (1.046 vs. 1.082; Fig. 4*E*). These differences can be explained simultaneously by the lifespan of radical pair under the theoretical framework of MIE. According to the MIE theory, MIF arises when the intermediate radical pairs have distinct chances to undergo triplet-singlet transition and recombine to the original reactant molecule (regeneration) for magnetic and nonmagnetic isotopes (5). Therefore, the magnitude of MIF and the ratio of MIF between magnetic isotopes (for example, $\Delta^{119}Sn/\Delta^{117}Sn$) depend on the lifespan for radicals (typical range: 10^{-10} to 10^{-8} s) relative to the conversion time of triplet-singlet transition for radical pairs (typical range: 10^{-9} to 10^{-6} s) (4, 25). For shorted-lived radicals, the ratios of MIF for magnetic isotopes are proportional to the square of the ratio of the magnetic moment of the isotope pair [e.g., for Sn isotopes, $\Delta^{119}Sn/\Delta^{117}Sn = (^{119}\mu_n/^{117}\mu_n)^2$], whereas for long-lived radical pairs, the MIF ratios are proportional to the square root of the magnetic moment of the isotope pair [e.g., $\Delta^{119}Sn/\Delta^{117}Sn = (^{119}\mu_n/^{117}\mu_n)^{0.5}$)] (10, 25).

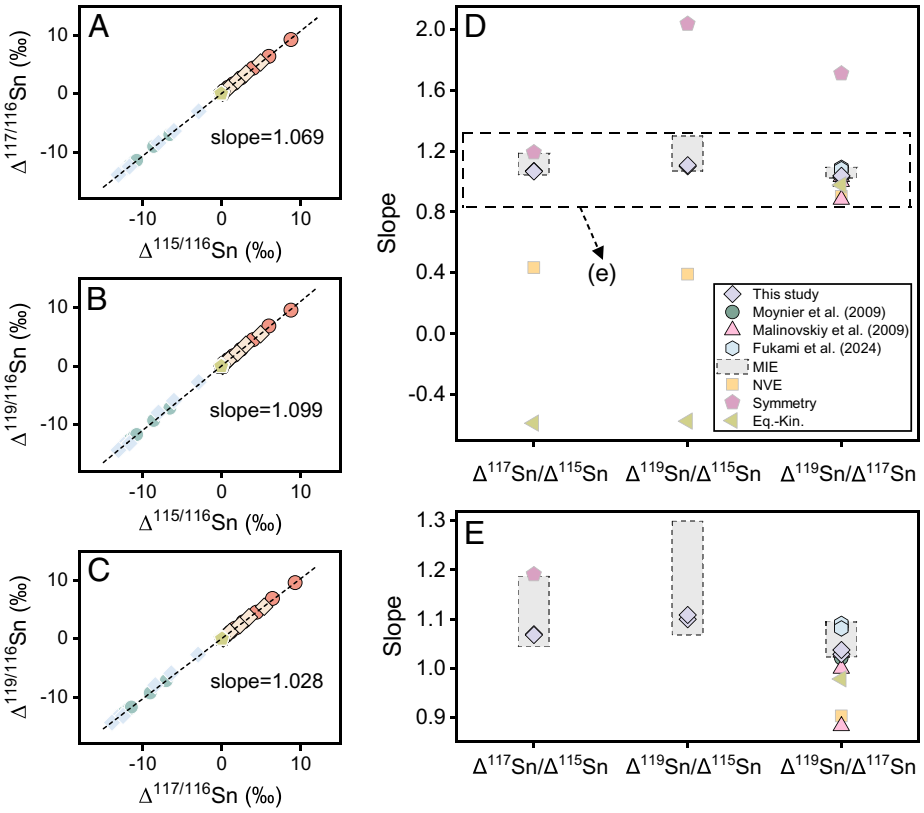

Fig. 4. Relationships between (*A*) $\Delta^{117/116}$Sn and $\Delta^{115/116}$Sn, (*B*) $\Delta^{119/116}$Sn and $\Delta^{115/116}$Sn, and (*C*) $\Delta^{119/116}$Sn and $\Delta^{117/116}$Sn obtained from photolysis experiments under the Earth's natural magnetic field. Dashed lines in panels (*A–C*) represent regression lines for each relationship. (*D* and *E*) Ratios of $\Delta^{117/116}$Sn/$\Delta^{115/116}$Sn, $\Delta^{119/116}$Sn/$\Delta^{115/116}$Sn, and $\Delta^{119/116}$Sn/$\Delta^{117/116}$Sn from photolysis experiments in this study, compared with $\Delta^{119/116}$Sn/$\Delta^{117/116}$Sn ratios from previous studies (7, 8, 10). Theoretical slopes for the nuclear volume effect (NVE) (21), magnetic isotope effect (MIE) (10), the symmetry effect (22), and the difference between the equilibrium and kinetic mass-dependent fractionation (14) are included. Panel e provides an enlargement of a portion of the data presented in panel *D*.

Long-lived radicals also facilitate increased singlet-triplet conversion and enhance the regeneration probabilities, thus amplifying the magnitude of MIF (25). The fact that our photochemical experiments yielded a greater span in Δ^{117}Sn and Δ^{119}Sn, but a smaller slope for Δ^{119}Sn/Δ^{117}Sn compared to transient liquid extraction experiments (10) can be attributed to a single reason of longer radical lifetimes during our photochemical experiments. Therefore, radical pair dynamics governed the Sn-MIF variability in our experimental systems.

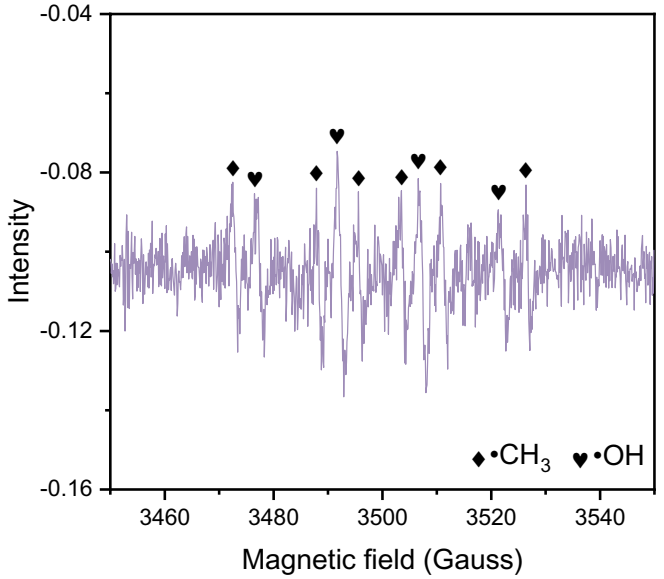

Fig. 5. Electron paramagnetic resonance (EPR) spectra of organic Sn solutions obtained from photolysis experiments using DMPO as a spin-trapping agent. Methyl radicals (•CH_3) are generated through homolytic cleavage of Sn–C bonds during UV photolysis, while hydroxyl radicals (•OH) emerge as secondary photoproducts in methyltin hydrolysis within aqueous environments.

The Magnetic Field Dependence of MIE. The magnetic field sensitivity of MIE for Mg, Ge, S, and Si was initially proposed in pioneering studies of Buchachenko (5, 11). However, subsequent research by Crotty (26) questioned the universality of MIE and magnetic field effects in enzymatic ATP synthesis, leaving this a topic of continuous debate. While magnetic interactions (~0.3 J/mol) are orders of magnitude weaker than thermal energies (2,400 J/mol) (25), they can modulate reaction rates by perturbing spin dynamics in radical pairs (25, 27). Our experiments provide solid evidence to resolve the debate: Sn-MIF magnitudes vary systematically with applied magnetic fields (0.002 to 3,255 G; Fig. 3), with reaction rates diverging significantly above 55 G (Fig. 3 and *SI Appendix*, Fig. S3). This direct correlation between magnetic field strength and mass-independent Sn isotope fractionation unequivocally demonstrates the MIE origin of Sn-MIF.

MIE originates from spin-selective recombination of radical pairs, where magnetic isotopes (e.g., ^{115}Sn, ^{117}Sn, ^{119}Sn) accelerate triplet-to-singlet intersystem crossing (ISC) (23). The ISC can be induced by hyperfine interaction (the interaction with the internal field of the magnetic nucleus) or Zeeman interaction (the interaction with the external magnetic field). In weak external fields comparable to the internal magnetic fields, the hyperfine interaction dominates ISC, enabling T_+, T_0, and T_- to S transitions. At stronger fields, the Zeeman effect suppresses HFC-driven ISC,

restricting transitions to T_0 – S and reducing MIE (4). Remarkably, Sn-MIF demonstrates dual maxima that are both lower than the HFC constant (A). Specifically, it exhibits an initial peak near 0.5 G (HFC-dominated regime) and a prominent peak at 444.4 G (Fig. 3), where the external field approximates the exchange interaction energy (J), inducing degeneracy between the singlet (S) and T_- states. This contrasts with Ge, C, and S isotopes, which peak at fields exceeding their HFC constants (A) (*SI Appendix*, Fig. S5)—a divergence potentially tied to differences in nuclear spin (I), radical pair lifetimes, or ligand environments. Critically, Sn-MIF's nonmonotonic field dependence (Fig. 3) reflects competition between HFC, Zeeman effect, and exchange interactions (4). Our study provides experimental evidence linking Sn-MIF to magnetic field-modulated spin dynamics, and the data await further quantitative interpretation by advanced quantum mechanical calculations to disentangle the roles of magnetic field, and spin/molecular/chemical dynamics in MIE systems.

Sensitivity of Sn-MIF to UV and Implications. The wavelength dependence of photochemical reactions, governed by the Grotthuss–Draper law that only absorbed light drives photolysis (28), critically modulates Sn-MIF. Under contemporary solar radiation ($\lambda > 290$ nm), Sn-MIF is absent, contrasting with Hg isotopes (2) but resembling S isotopes (29). This discrepancy arises because atmospheric O_2 and O_3 absorb UV below 290 nm (30), leaving surface sunlight devoid of the 190 to 240 nm wavelength range required for organotin photolysis to generate radical pairs (*SI Appendix*, Fig. S6). Present-day methyltin photolysis thus proceeds via direct bond cleavage (*SI Appendix*, Fig. S4), bypassing spin-selective radical recombination pathways and suppressing Sn-MIF entirely.

Atmospheric chemistry (e.g., O_2 and CO_2 levels) is a key factor in planetary habitability, regulating the nutrient cycle, climate dynamics, and life's emergence (31, 32). During the Archean, low atmospheric O_2 permitted methane-driven photochemistry to dominate, sustaining a habitable climate under faint young Sun conditions (33). The Great Oxidation Event (GOE, ~2.3 Ga) marked a critical transition during which methane oxidation altered atmospheric composition (33), potentially triggering Snowball Earth episodes (34). While mass-independent sulfur isotope fractionation (S-MIF) placed strong constraints on atmospheric O_2 history (35), our finding of Sn-MIF introduces a complementary tracer. Our experiments indicate that Sn-MIF could have occurred prior to GOE but should have diminished thereafter. This binary behavior positions Sn-MIF as a unique tracer for pinpointing the GOE's timing and intensity. Beyond Earth, Sn-MIF could trace past photochemical activity on Mars, akin to ^{13}C-depleted Martian organics (36, 37). Sn-MIF thus may serve not only as a proxy of atmospheric oxygen level but also as a biosignature for prebiotic metal–organics interaction, offering insights into extraterrestrial chemical evolution.

To harness Sn-MIF's diagnostic power, targeted analyses of key archives are crucial. Archean organic-rich shales, banded iron formations (BIFs), and sulfides are the potential hosts of Sn^{2+} species or organotin complexes. Although Archean seawater Sn concentrations were likely ultralow (<1 ng/g) (38, 39), Fe oxides in BIFs can exhibit Sn enrichment factors up to 10^7 (40), offering viable reservoirs for Sn-MIF preservation. Sn-MIF signatures may also be archived via adsorption onto clay minerals (41, 42) in shales or sequestration within sulfide phases (e.g., stannite), mirroring sulfur MIF preservation pathways (43, 44). Based on our experiments, positive Sn-MIF signatures (i.e., $\Delta^{117}Sn$) may be found in organic-rich shales, whereas negative $\Delta^{117}Sn$ values may be measured from inorganic sinks like BIFs or sulfides. Also, as implied by our experiments, post-GOE ozone formation should have suppressed the terrestrial Sn-MIF, leaving only mass-dependent fractionation in Phanerozoic coals (45) and modern sediments (46, 47), despite ongoing organotin photodegradation (12, 48). Extraterrestrially, Martian meteorites exposed to intense UV flux under a thin atmosphere (49) may preserve Sn-MIF in sulfides and organic-rich lithologies due to limited crustal recycling, analogous to S-MIF's role in elucidating Mars' atmospheric photochemistry (29, 50).

Due to the relatively low Sn concentrations in Archean sediments and meteorites (0.5 to 10 μg/g) (51, 52), historical analytical limitations left Sn-MIF signatures underexplored. However, recent advances in chemical separation techniques and MC-ICP-MS instrumentation now enable precise (±0.01‰ per mass unit) Sn isotope analysis at ultratrace levels (i.e., 1 ng/g Sn in samples) (6, 53, 54). Future studies may further explore mineral-scale analyses via laser ablation MC-ICP-MS (LA-MC-ICP-MS) or secondary ion mass spectrometry (SIMS), which will avoid the dilution of isotopic anomalies inherent in bulk-rock measurements (29, 55). By integrating MIF signatures of Sn, S, and Hg isotope systems (56) into studies of terrestrial sediments and Martian meteorites, we could establish multiproxy frameworks to decode planetary photochemistry evolution. Therefore, by pairing MIF-targeted Sn isotope analyses of natural samples with experimental calibrations under simulated planetary UV fluxes, we may realize the potential of Sn-MIF to provide insights into atmospheric evolution on Earth and other planets.

Materials and Methods

Materials and Reagents. All chemical treatments of samples were performed at the State Key Laboratory of Critical Earth Material Cycling and Mineral Deposits, Nanjing University. The semiconductor-grade acids (HCl, HNO_3, HF) and ultrapure water (18.25 MΩ) were used for sample preparation and ion-exchange chromatography. Analytical-grade methyltin trichloride, $SnCl_2{\cdot}2H_2O$, $SnCl_4{\cdot}5H_2O$, DMPO (5,5-dimethyl-1-pyrroline N-oxide, $C_6H_{11}NO$) were sourced from Alfa Aesar@ and Macklin@. Pure Sn elemental standard solutions were used as in-house standards, including NIST 3161a (Lot #140917), SPEX (Lot #2219SNY), and $SnCl_4$ solutions. For photolysis experiments, quartz glass vessels were employed, which were soaked in 50% HNO_3 and deionized water and subsequently cleaned with three rinses of deionized water.

Photolysis Experiments. Photolysis of methyltin trichlorides [$Sn(CH_3)Cl_3$] was performed in quartz vessels. Before each experiment, a solution with a pH of ~0.3 was prepared by adding 16.67 mL MQ water with 0.02 mL 0.1 M HCl to the vessel, followed by adding 3.33 mL 1,200 ug/g $Sn(CH_3)Cl_3$ (PR2, PR42). The $Sn(CH_3)Cl_3$ stock solution was prepared by dissolving 100 mg $Sn(CH_3)Cl_3$ powder in 40 mL MQ water. In the DMPO experiment (PR68), approximately 10 mg of DMPO was added to the reaction system.

All UV irradiation experiments were conducted using a medium-pressure mercury lamp (MP-Hg) with a maximum emission at 365 nm (*SI Appendix*, Figs. S1 and S6). The lamp was positioned approximately 10 cm from the reaction vessel, and the light intensity was measured using a radiometer equipped with sensors specific to MP-Hg lamps. The spectral output of the lamp was characterized using a UV-vis spectrophotometer (UV-2700, Shimadzu, Japan). A rotating disk photoreactor equipped with the MP-Hg lamp was used for all experiments, which were carried out at room temperature (25 °C). For experiments simulating natural photochemical conditions, the Hg lamp was replaced with unfiltered natural sunlight. The irradiation setup was positioned outdoors (Nanjing, China) under clear-sky conditions. The quartz vessels were sealed with plugs to prevent contamination. Subsamples were collected from the reacting solution at regular intervals and transferred to clean polypropylene tubes, which were then covered with aluminum foil. The samples were acidified with 4 mL of 1.05 M HCl.

For conducting magnetic field experiments, we utilized a specialized movable Hg light source equipped with a cooling fan to perform identical photolysis experiments under various magnetic field conditions (*SI Appendix*, Fig. S1).

The experimental solution was uniformly prepared by first adding 16.67 mL of MQ water and 0.02 mL of 0.1 M HCl to a container, followed by the addition of 3.33 mL of a 1,200 ug/g $Sn(CH_3)Cl_3$ solution (including PR37, as well as 61, 64, 72, and 76 to 95). The direct current power supply used was model PS-3010, which features a coil tube capable of accommodating a maximum input current of 8 A. Based on the current-magnetic field relationship (H = 826.6*I + 30.6), this setup can generate a maximum magnetic field of 4,150 G, where I represents the current and H represents the resulting magnetic field. To mitigate the potential heating of the sample, it was recommended to use a current lower than 6 A and to operate the magnet for less than 10 h. Furthermore, one of the experiments was conducted in a paleomagnetic laboratory with a field strength of 0.002 G. A 25-mL quartz reaction tube filled with 20 mL of the reaction solution was placed at the center of the magnet. All magnetic fields were verified using a probe gaussmeter, while the reaction temperature was maintained by an air conditioner and occasionally monitored.

Separation of Organic and Inorganic Sn. The chemical separation of organic and inorganic Sn was performed using 1 mL AG MP-1 resin, as detailed in the *SI Appendix*, Table S1. The column was cleaned with alternating volumes of MQ water and 0.5 M HNO_3. Sample in 2 mL of 1.05 M HCl was loaded on the columns and rinsed with 5 mL of 1.05 M HCl and 2 mL of 0.5 M HCl to collect organic Sn. To obtain the inorganic Sn fraction, 10 μL of HF was added to the collection beakers before rinsing with 6 mL 0.5 M HNO_3. The efficiency of the chemical separation procedure was verified with pure inorganic Sn, pure organic Sn (methyltin), and a mixture of both. The results showed that the yield of organic Sn was greater than 97%, while the yield of inorganic Sn was greater than 99%, confirming the effectiveness of the separation method.

EPR Analysis. The electron paramagnetic resonance (EPR) spectra were recorded using a Bruker EMX/plus spectrometer (E500-9.5/12, Germany) with a movable MP-Hg lamp for in situ irradiation. The center field, sweep width, sweep time, conversion time, modulation field amplitude, frequency, microwave power, and sweep scan were set at 3,500 G, 200 G, 30 s, 30 ms, 1 G, 100 kHz, 2 mW, and 6 (57). The sample mixed with 5,5-dimethyl-1-pyrroline-N-oxide (DMPO) was injected into a fused silica capillary tube with one side sealed and placed inside a quartz tube within the EPR system. After several minutes of irradiation, the EPR signals of the sample were collected. The background was corrected by using the signal of the solution without irradiation.

Sn elemental Analysis. Elemental concentrations were analyzed using inductively coupled plasma optical emission spectrometry (ICP-OES) with a Skyray ICP-3000 instrument. A series of gravimetrically prepared multielement standards (0.01 to 20 μg/g) were used for calibration and instrument drift correction. An independent 1 ug/g standard solution was bracketed between five to ten samples to monitor the stability of the instrument. External precision of the elemental analysis was better than 10% (2 relative SD).

Sn Isotope Analysis. All Sn isotope analysis of solutions from the photolysis experiments was performed using a Nu 1700 Sapphire multicollector inductively coupled plasma mass spectrometer (MC-ICP-MS) at the State Key Laboratory of Critical Earth Material Cycling and Mineral Deposits, Nanjing University. The instrument was operated at middle resolution under wet plasma, with detailed instrument settings and operational parameters summarized in the *SI Appendix*, Table S2. The samples were measured using elemental doping and sample-standard bracketing under wet plasma conditions. The 1 ug/g Sn solution was doped with 300 ng/g Sb and was introduced into ICP by a standard glass spray chamber via a 100 μL/min PFA nebulizer. The typical signal intensities for ^{120}Sn and ^{121}Sb were ~10 and ~8 V per μg/g. Measurement of blanks was performed at the beginning of every session and corrected for both standards and samples. Between each isotope analysis, the sample introduction system was washed by uptaking 0.3 M HNO3-0.006 M HF solutions sequentially from three tubes, each for 40 seconds. In an analytical session, every sample was bracketed by a NIST 3161a standard at the same concentration. Data reduction of Sn isotope analysis for this method was similar to a previous study (58).

All isotopic results are expressed as $\delta^{X/116}Sn$ notation relative to the primary Sn isotopic reference solution NIST 3161a in this study, which is $\delta^{X/116}Sn = [(^{X}Sn/^{116}Sn)_{sample}/(^{X}Sn/^{116}Sn)_{3161a} - 1] \times 1{,}000$, where X indicates 115, 117, 118, 119, 120, 122. $\Delta^{X/116}Sn$ denotes the measured $\delta^{X/116}Sn$ corrected by $\delta^{120/116}Sn$ using the kinetic fractionation law (14). The external reproducibility of the Sn isotope analysis was determined to be 0.15‰ for $\delta^{115/116}Sn$, 0.04‰ for $\delta^{117/116}Sn$, 0.07‰ for $\delta^{118/116}Sn$, 0.10‰ for $\delta^{119/116}Sn$, 0.12‰ for $\delta^{120/116}Sn$, 0.16‰ for $\delta^{122/116}Sn$, 0.14‰ for $\Delta^{115/116}Sn$, 0.03‰ for $\Delta^{117/116}Sn$, 0.02‰ for $\Delta^{118/116}Sn$, 0.03‰ for $\Delta^{119/116}Sn$, and 0.06‰ for $\Delta^{122/116}Sn$ using the repeated analyses of NIST 3161a.

Data, Materials, and Software Availability. All study data are included in the article and/or supporting information.

ACKNOWLEDGMENTS. We thank Yongxiang Li, Xinyu Liu, and Guoyang Zhang for their help with the experiments. This study was supported by National Natural Science Foundation of China (42425301 to W.L., 42403009 to J.-X.S.), Jiangsu Funding Program for Excellent Postdoctoral Talent (Grant Number: 375928), Key Laboratory of Marine Mineral Resources, Ministry of Natural Resources, Guangzhou (Grant Number: KLMMR-2024-K01) to J.-X.S., Frontiers Science Center for Critical Earth Material Cycling, Nanjing University (Grant Number: DLTD2103), China National Space Administration (Grant Number: D020205) to W.L.

1. M. Amor *et al.*, Mass-dependent and -independent signature of Fe isotopes in magnetotactic bacteria. *Science* **352**, 705–708 (2016).
2. B. A. Bergquist, J. D. Blum, Mass-dependent and -independent fractionation of Hg isotopes by photoreduction in aquatic systems. *Science* **318**, 417 (2007).
3. A. L. Buchachenko, Magnetic isotopes as a means to elucidate Earth and environmental chemistry. *Russ. Chem. Rev.* **87**, 727–740 (2018).
4. K. M. M. Salikhov, N. Yu, R. Z. Sagdeev, A. L. Buchachenko, "Spin polarization and magnetic effects in radical reactions" in *Studies in Physical and Theoretical Chemistry* (Elsevier, Amsterdam, 1984), **vol. 22**.
5. A. L. Buchachenko, Magnetic isotope effect: Nuclear spin control of chemical reactions. *J. Phys. Chem. A* **105**, 9995–10011 (2001).
6. A. Bragagni, F. Wombacher, M. Kirchenbaur, N. Braukmüller, C. Münker, Mass-independent Sn isotope fractionation and radiogenic 115Sn in chondrites and terrestrial rocks. *Geochim. Cosmochim. Acta* **344**, 40–58 (2023).
7. F. Moynier, T. Fujii, P. Telouk, Mass-independent isotopic fractionation of tin in chemical exchange reaction using a crown ether. *Anal. Chimica Acta* **632**, 234–239 (2009).
8. D. Malinovskiy, L. Moens, F. Vanhaecke, Isotopic fractionation of Sn during methylation and demethylation reactions in aqueous solution. *Environ. Sci. Technol.* **43**, 4399–4404 (2009).
9. A. L. Buchachenko, V. A. Roznyatovskii, V. L. Ivanov, Y. A. Ustynyuk, Chemically induced magnetic isotope effect on the tin nuclei during the photolysis of (1-fluorenyl)trimethyltin. *Russ. J. Phys. Chem.* **80**, 1009–1010 (2006).
10. Y. Fukami *et al.*, Variation in the relationship between odd isotopes of tin in mass-independent fractionation induced by the magnetic isotope effect. *Proc. Natl. Acad. Sci.* **121**, e2321616121 (2024).
11. A. L. Buchachenko, A. A. Bukhvostov, K. V. Ermakov, D. A. Kuznetsov, A specific role of magnetic isotopes in biological and ecological systems. Physics and biophysics beyond. *Prog. Biophys. Mol. Biol.* **155**, 1–19 (2020).
12. M. Hoch, Organotin compounds in the environment: An overview. *Appl. Geochem.* **16**, 719–743 (2001).
13. K. Dubalska, M. Rutkowska, G. Bajger-Nowak, P. Konieczka, J. Namieśnik, Organotin compounds: Environmental fate and analytics. *Crit. Rev. Anal. Chem.* **43**, 35–54 (2013).
14. E. D. Young, A. Galy, H. Nagahara, Kinetic and equilibrium mass-dependent isotope fractionation laws in nature and their geochemical and cosmochemical significance. *Geochim. Cosmochim. Acta* **66**, 1095–1104 (2002).
15. M. V. Ivanov, D. Babikov, On molecular origin of mass-independent fractionation of oxygen isotopes in the ozone forming recombination reaction. *Proc. Natl. Acad. Sci. U.S.A.* **110**, 17708–17713 (2013).
16. J. E. Heidenreich III, M. H. Thiemens, A non-mass-dependent oxygen isotope effect in the production of ozone from molecular oxygen: The role of molecular symmetry in isotope chemistry. *J. Chem. Phys.* **84**, 2129–2136 (1986).
17. E. A. Schauble, Role of nuclear volume in driving equilibrium stable isotope fractionation of mercury, thallium, and other very heavy elements. *Geochim. Cosmochim. Acta* **71**, 2170–2189 (2007).
18. V. N. Epov, Magnetic isotope effect and theory of atomic orbital hybridization to predict a mechanism of chemical exchange reactions. *Phys. Chem. Chem. Phys.* **13**, 13222 (2011).
19. V. N. Epov, D. Malinovskiy, F. Vanhaecke, D. Bégué, O. F. X. Donard, Modern mass spectrometry for studying mass-independent fractionation of heavy stable isotopes in environmental and biological sciences. *J. Anal. At. Spectrom.* **26**, 1142–1156 (2011).
20. E. A. Schauble, Modeling nuclear volume isotope effects in crystals. *Proc. Natl. Acad. Sci.* **110**, 17714 (2013).
21. I. Angeli, K. P. Marinova, Table of experimental nuclear ground state charge radii: An update. *Atomic Data Nuclear Data Tables* **99**, 69–95 (2013).
22. F. Robert, P. Reinhardt, Mass independent isotopic fractionation: A key to plasma chemistry. *Chem. Phys. Impact* **4**, 100073 (2022).
23. N. J. Turro, Influence of nuclear spin on chemical reactions: Magnetic isotope and magnetic field effects (A Review). *Proc. Natl. Acad. Sci.* **80**, 609 (1983).
24. K. P. Madden, H. Taniguchi, The role of the DMPO-hydrated electron spin adduct in DMPO-OH spin trapping. *Free Radic. Biol. Med.* **30**, 1374–1380 (2001).

25. A. L. Buchachenko, *Magnetic Isotope Effect in Chemistry and Biochemistry* (Nova Science Publishers, NY, 2009).
26. D. Crotty *et al.*, Reexamination of magnetic isotope and field effects on adenosine triphosphate production by creatine kinase. *Proc. Natl. Acad. Sci.* **109**, 1437–1442 (2012).
27. I. R. Gould, N. J. Turro, M. B. Zimmt, "Magnetic field and magnetic isotope effects on the products of organic reactions" in *Advances in Physical Organic Chemistry*, V. Gold, D. Bethell, Eds. (Academic Press, 1984), vol. 20, pp. 1–53.
28. J. P. Menzel, B. B. Noble, J. P. Blinco, C. Barner-Kowollik, Predicting wavelength-dependent photochemical reactivity and selectivity. *Nat. Commun.* **12**, 1691 (2021).
29. J. Farquhar, H. Bao, M. Thiemens, Atmospheric influence of Earth's earliest sulfur cycle. *Science* **289**, 756 (2000).
30. M. W. Claire *et al.*, Modeling the signature of sulfur mass-independent fractionation produced in the Archean atmosphere. *Geochim. Cosmochim. Acta* **141**, 365–380 (2014).
31. G. Y. Wei, G. Li, Atmospheric oxygenation as a potential trigger for climate cooling. *Sci. Bull.* **69**, 3717–3722 (2024).
32. D. E. Canfield, The early history of atmospheric oxygen: Homage to Robert M. Garrels. *Annu. Rev. Earth Planet. Sci.* **33**, 1–36 (2005).
33. T. W. Lyons, C. T. Reinhard, N. J. Planavsky, The rise of oxygen in Earth's early ocean and atmosphere. *Nature* **506**, 307–315 (2014).
34. P. F. Hoffman, The great oxidation and a Siderian snowball Earth: MIF-S based correlation of Paleoproterozoic glacial epochs. *Chem. Geol.* **362**, 143–156 (2013).
35. C. T. Reinhard, N. J. Planavsky, Biogeochemical controls on the redox evolution of Earth's oceans and atmosphere. *Elements* **16**, 191–196 (2020).
36. Y. Ueno *et al.*, Synthesis of 13C-depleted organic matter from CO in a reducing early Martian atmosphere. *Nature Geosci.* **17**, 503–507 (2024).
37. J. Alday *et al.*, Photochemical depletion of heavy CO isotopes in the Martian atmosphere. *Nat. Astron.* **7**, 867–876 (2023).
38. S. A. Abdel Ghani, Trace metals in seawater, sediments and some fish species from Marsa Matrouh beaches in north-western Mediterranean coast, Egypt. *Egypt. J. Aquat. Res.* **41**, 145–154 (2015).
39. J. T. Byrd, M. O. Andreae, Tin and methyltin species in seawater: Concentrations and fluxes. *Science* **218**, 565–569 (1982).
40. J. Ren *et al.*, Ultraselective enrichment of trace elements in seawater by Co-rich ferromanganese nodules. *Glob. Planet. Change* **239**, 104498 (2024).
41. D. Durce, S. Salah, L. Wang, N. Maes, Complexation of Sn with Boom Clay natural organic matter under nuclear waste repository conditions. *Appl. Geochem.* **123**, 104775 (2020).
42. D. Durce *et al.*, Sn(IV) sorption onto illite and Boom clay: Effect of carbonate and dissolved organic matter. *Minerals* **12**, 1078 (2022).
43. S. Ono *et al.*, New insights into Archean sulfur cycle from mass-independent sulfur isotope records from the Hamersley Basin, Australia. *Earth Planet. Sci. Lett.* **213**, 15–30 (2003).
44. B. Eickmann *et al.*, Isotopic evidence for oxygenated Mesoarchaean shallow oceans. *Nature Geosci.* **11**, 133–138 (2018).
45. Q. Qu *et al.*, Tin stable isotopes in magmatic-affected coal deposits: Insights in the geochemical behavior of tin. *Appl. Geochem.* **119**, 104641 (2020).
46. D. Cao, G. Jiang, Q. Zhou, R. Yang, Organotin pollution in China: An overview of the current state and potential health risk. *J. Environ. Manage.* **90**, S16–S24 (2009).
47. Z. Chen *et al.*, Organotin contamination in sediments and aquatic organisms from the yangtze estuary and adjacent marine environments. *Environ. Eng. Sci.* **34**, 227–235 (2017).
48. J. Wang *et al.*, Insights into the crystallinity-dependent photochemical productions of reactive oxygen species from iron minerals. *Environ. Sci. Technol.* **58**, 10623–10631 (2024).
49. D. M. Hassler *et al.*, Mars' surface radiation environment measured with the Mars Science Laboratory's Curiosity rover. *Science* **343**, 1244797 (2014).
50. S. W. Poulton *et al.*, A 200-million-year delay in permanent atmospheric oxygenation. *Nature* **592**, 232–236 (2021).
51. J. B. Creech, F. Moynier, Tin and zinc stable isotope characterisation of chondrites and implications for early Solar System evolution. *Chem. Geol.* **511**, 81–90 (2019).
52. A. J. Boyd, M. T. Rosing, M. A. R. Harding, D. E. Canfield, T. Hassenkam, 3.7 billion year old detrital sediments in Greenland are consistent with active plate tectonics in the Eoarchean. *Commun. Earth Environ.* **5**, 201 (2024).
53. W. Song *et al.*, High-precision Sn isotopic measurement in geological materials by double-spike MC-ICP-MS. *Geostand. Geoanal. Res.* **49**, 245–258 (2024), 10.1111/ggr.12590.
54. Q. Qu *et al.*, A novel chemical purification method for accurate Sn isotope measurement by MC-ICP-MS. *J. Anal. At. Spectrom.* **39**, 2258–2269 (2024).
55. J. Farquhar, M. H. Thiemens, T. Jackson, Atmosphere-Surface Interactions on Mars: Δ17O Measurements of Carbonate from ALH 84001. *Science* **280**, 1580–1582 (1998).
56. A. L. Zerkle *et al.*, Sulfur and mercury MIF suggest volcanic contributions to Earth's atmosphere at 2.7 Ga. *Geochem. Perspect. Lett.* **18**, 48–52 (2021).
57. Z. Sun *et al.*, Roles of natural phenolic compounds in polycyclic aromatic hydrocarbons abiotic attenuation at soil–air interfaces through oxidative coupling reactions. *Environ. Sci. Technol.* **57**, 11967–11976 (2023).
58. J.-X. She, W. Li, S. An, T. Yang, R. Zhang, In situ Sn isotope analysis of cassiterite (SnO2) by nanosecond laser ablation MC-ICP-MS. *J. Anal. At. Spectrom.* **38**, 1043–1056 (2023).